

# Three-Dimensional $\text{LiMnPO}_4 \cdot \text{Li}_3\text{V}_2(\text{PO}_4)_3/\text{C}$ Nanocomposite as a Bicontinuous Cathode for High-Rate and Long-Life Lithium-Ion Batteries

Yanzhu Luo,<sup>†</sup> Xu Xu,<sup>†</sup> Yuxiang Zhang,<sup>‡</sup> Yuqiang Pi,<sup>‡</sup> Mengyu Yan,<sup>†</sup> Qiulong Wei,<sup>†</sup> Xiacong Tian,<sup>†</sup> and Liqiang Mai<sup>\*,†</sup>

<sup>†</sup>State Key Laboratory of Advanced Technology for Materials Synthesis and Processing, Wuhan University of Technology, Wuhan 430070, P. R. China

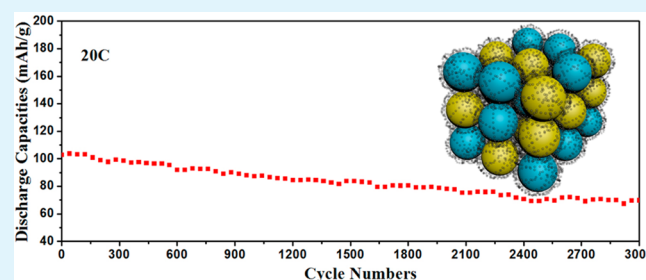
<sup>‡</sup>WUT Powerful Energy Company, Ltd., Wuhan 430223, P. R. China

## Supporting Information

**ABSTRACT:** Olivine-type  $\text{LiMnPO}_4$  has been extensively studied as a high-energy density cathode material for lithium-ion batteries. To improve both the ionic and electronic conductivities of  $\text{LiMnPO}_4$ , a series of carbon-decorated  $\text{LiMnPO}_4 \cdot \text{Li}_3\text{V}_2(\text{PO}_4)_3$  nanocomposites are synthesized by a facile sol–gel method combined with the conventional solid-state method. The optimized composite presents a three-dimensional hierarchical structure with active nanoparticles well-embedded in a conductive carbon matrix. The combination of the nanoscale carbon coating and the microscale carbon network could provide a more active site for electrochemical

reaction, as well as a highly conductive network for both electron and lithium-ion transportation. When cycled at 20 C, an initial specific capacity of  $103 \text{ mA h g}^{-1}$  can be obtained and the capacity retention reaches 68% after 3000 cycles, corresponding to a capacity fading of 0.013% per cycle. The stable capacity and excellent rate capability make this carbon-decorated  $\text{LiMnPO}_4 \cdot \text{Li}_3\text{V}_2(\text{PO}_4)_3$  nanocomposite a promising cathode for lithium-ion batteries.

**KEYWORDS:** lithium–manganese phosphate, lithium–vanadium phosphate, high rate, long life, lithium-ion diffusion



## 1. INTRODUCTION

As an important member of olivine-type lithium transition-metal phosphates  $\text{LiMPO}_4$  ( $M = \text{Fe}, \text{Mn}$ ),  $\text{LiMnPO}_4$  has been extensively studied as a promising cathode material for lithium-ion batteries because of its high energy density, low toxicity, and relatively low cost.<sup>1–4</sup>  $\text{LiMnPO}_4$  exhibits a higher potential plateau (4.10 V vs  $\text{Li}/\text{Li}^+$ ) than  $\text{LiFePO}_4$  (3.45 V vs  $\text{Li}/\text{Li}^+$ ), providing about 20% higher energy density ( $701 \text{ Wh kg}^{-1}$ ) than  $\text{LiFePO}_4$  ( $586 \text{ Wh kg}^{-1}$ ).<sup>5,6</sup> Moreover, the voltage range of  $\text{LiMnPO}_4$  is compatible with the currently commercialized organic electrolytes for lithium-ion batteries, which makes it more easily utilized in practical applications with high energy density.<sup>5,7</sup>

However,  $\text{LiMnPO}_4$  suffers from extremely low ionic ( $\sim 10^{-15} \text{ cm}^2 \text{ s}^{-1}$ ) and electronic ( $< 10^{-10} \text{ S cm}^{-1}$ ) conductivities, Jahn–Teller effect of  $\text{Mn}^{3+}$  ion, passivation phenomenon upon delithiation, metastable nature of  $\text{MnPO}_4$ , and large volume change caused by interface strain between the  $\text{LiMnPO}_4/\text{MnPO}_4$  phases during charge/discharge processes.<sup>8–10</sup> As a result, the pure  $\text{LiMnPO}_4$  shows low capacity, high polarization, poor rate performance, and limited cycle life.<sup>11</sup> In order to improve the rate capability of  $\text{LiMnPO}_4$ , various strategies have been proposed, such as downsizing the particle size,<sup>10,12</sup> cationic doping,<sup>5,8,11</sup> and carbon coating.<sup>13,14</sup>

Vanadium is a particularly attractive element for constructing a number of electrochemically active compounds, such as  $\text{Li}_3\text{V}_2(\text{PO}_4)_3$ ,<sup>5,15,16</sup> which can provide a three-dimensional (3D) pathway for  $\text{Li}^+$  insertion/extraction, allowing fast transport of lithium ions.<sup>17–19</sup> Qin et al.<sup>5</sup> synthesized the  $(1-x)\text{LiMnPO}_4 \cdot x\text{Li}_3\text{V}_2(\text{PO}_4)_3/\text{C}$  ( $x = 0, 0.1, 0.2, 0.3, 0.4, 0.5, 1$ ) nanocomposites through the solid-state method, and  $0.6\text{LiMnPO}_4 \cdot 0.4\text{Li}_3\text{V}_2(\text{PO}_4)_3$  delivers the highest capacity of  $154 \text{ mA h g}^{-1}$  at 0.05 C. Wang et al.<sup>15</sup> also prepared a variety of  $x\text{LiMnPO}_4 \cdot y\text{Li}_3\text{V}_2(\text{PO}_4)_3/\text{C}$  ( $x:y = 8:1, 4:1, 2:1, \text{ and } 1:1$ ) nanocomposites by spray drying combined with the solid-state reaction. They found that the incorporation of  $\text{Li}_3\text{V}_2(\text{PO}_4)_3$  with  $\text{LiMnPO}_4$  could effectively enhance the electrochemical kinetics of the  $\text{LiMnPO}_4$  phase via the structure modification and shortened the lithium diffusion length in  $\text{LiMnPO}_4$ . Zhang et al.<sup>16</sup> demonstrated a carbon-coated  $\text{LiMnPO}_4 \cdot \text{Li}_3\text{V}_2(\text{PO}_4)_3$  composite cathode material with rodlike  $\text{MnV}_2\text{O}_6 \cdot 4\text{H}_2\text{O}$  as the precursor, which shows a good rate capability of  $80.4 \text{ mA h g}^{-1}$  at 10 C. Although the doping structure is carefully

Received: June 19, 2015

Accepted: July 21, 2015

Published: July 21, 2015

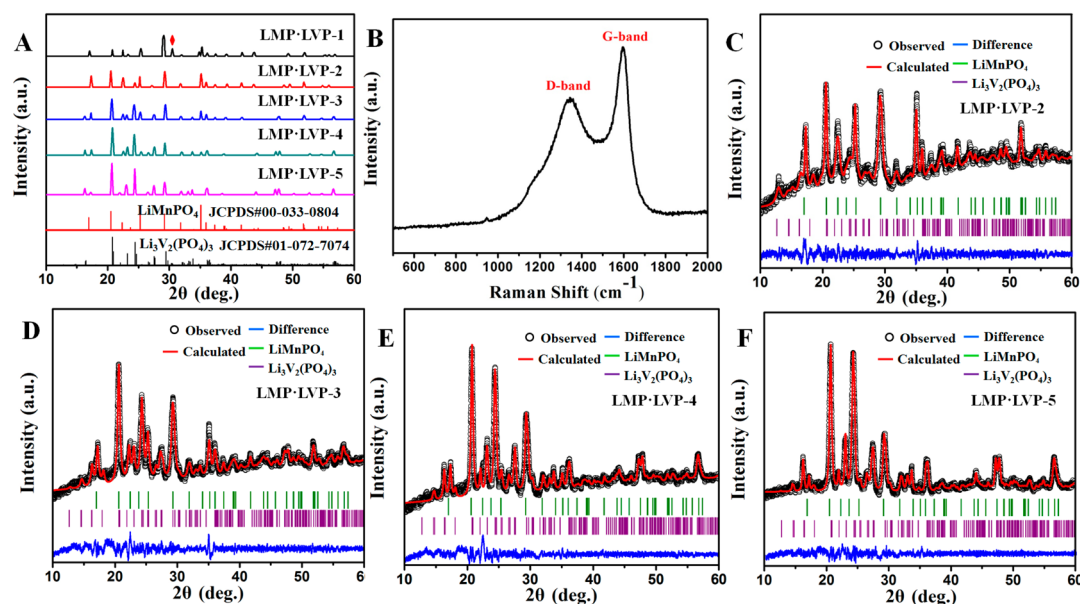


**Figure 1.** (A) XRD patterns of the  $n\text{LiMnPO}_4 \cdot (1 - n)\text{Li}_3\text{V}_2(\text{PO}_4)_3$  samples with different molar ratios. (B) Raman scattering spectrum of LMP-LVP-3. Rietveld refinement XRD patterns of LMP-LVP-2 (C), LMP-LVP-3 (D), LMP-LVP-4 (E), and LMP-LVP-5 (F).

investigated, the electrochemical properties of vanadium-modified  $\text{LiMnPO}_4$  at high rates are still unsatisfactory.

Uniform carbon coating on the particle surface is considered as an economic and feasible technique to enhance the electronic conductivity.<sup>20,21</sup> However, the common carbon coating could only provide the electrical pathway for an individual nanoparticle. When the active materials are embedded in a conductive carbon matrix, the homogeneity of the particle size and distribution would be greatly improved, which is critical for the electrochemical performance.<sup>22–24</sup> In consideration of the factors described above, the architecture combining the nanoscale carbon coating and the microscale carbon network is beneficial for the electrode material, which could provide more active site for electrochemical reaction, as well as a highly conductive network for both electron and lithium-ion transportation,<sup>25</sup> resulting in a higher capacity and better rate performance.

Here, we develop a facile method to prepare a series of  $n\text{LiMnPO}_4 \cdot (1 - n)\text{Li}_3\text{V}_2(\text{PO}_4)_3/\text{C}$  nanocomposites as the cathode materials. When  $n$  decreases to 0.6, the cathode materials with the composition of  $0.6\text{LiMnPO}_4 \cdot 0.4\text{Li}_3\text{V}_2(\text{PO}_4)_3/\text{C}$  present a hierarchical structure with active particles well-embedded in a conductive carbon matrix. The obtained cathode materials achieve an enhanced rate capability ( $103 \text{ mA h g}^{-1}$  at 20 C) and superior cycling stability (68% retention after 3000 cycles at 20 C), indicating their superiority in practical applications.

## 2. EXPERIMENTAL DETAILS

The 3D hierarchical  $n\text{LiMnPO}_4 \cdot (1 - n)\text{Li}_3\text{V}_2(\text{PO}_4)_3/\text{C}$  ( $n = 1, 0.8, 0.6, 0.4, \text{ and } 0.2$ ) nanocomposites were synthesized by a simple sol-gel method combined with the conventional solid-state method (Figure S1). Stoichiometric amounts of vanadium pentoxide ( $\text{V}_2\text{O}_5$ ) and oxalic acid ( $\text{H}_2\text{C}_2\text{O}_4$ ) were dissolved in deionized water at 80 °C for 15 min (molar ratio of  $\text{V}_2\text{O}_5/\text{H}_2\text{C}_2\text{O}_4 = 1:3$ ).<sup>20</sup> After the formation of a transparent blue solution of  $\text{VOC}_2\text{O}_4$ , manganese acetate tetrahydrate [ $(\text{CH}_3\text{COO})_2\text{Mn} \cdot 4\text{H}_2\text{O}$ ], phosphoric acid ( $\text{H}_3\text{PO}_4$ ), lithium acetate ( $\text{CH}_3\text{COOLi}$ ), and glucose ( $\text{C}_6\text{H}_{12}\text{O}_6$ ) were added into the above solution successively. Then, the obtained precursor solution was dried at 120 °C in an air oven, followed by calcination at

350 °C for 5 h in a nitrogen atmosphere to get a brown intermediate product. Finally, the brown powder was sintered at 700 °C for 8 h in a nitrogen atmosphere to yield the final product. The final products were designated as LMP-LVP-1 to LMP-LVP-5 ( $n\text{LiMnPO}_4 \cdot (1 - n)\text{Li}_3\text{V}_2(\text{PO}_4)_3/\text{C}$ , with  $n = 1, 0.8, 0.6, 0.4, \text{ and } 0.2$ ), respectively.

The crystal structures of  $n\text{LiMnPO}_4 \cdot (1 - n)\text{Li}_3\text{V}_2(\text{PO}_4)_3/\text{C}$  nanocomposites were analyzed by powder X-ray diffraction (XRD; Bruker D8 Advance) with a nonmonochromated  $\text{Cu K}\alpha$  X-ray source. Field-emission scanning electron microscopy (FESEM; JEOL JSM-7100F, 10 kV) and high-resolution transmission electron microscopy (HRTEM; JEOL JEM-2100F, 200 kV) were applied to characterize the morphologies and element distribution of all of the samples. The property of the carbon layer was analyzed with an INVIA Raman spectrometer. The specific surface area and Barrett–Joyner–Halenda (BJH) pore-size distribution were analyzed using a Micromeritics Tristar 3020 instrument.

To make the electrodes, 70% active materials were ground with 20% acetylene black and 10% poly(tetrafluoroethylene) to get circular disks with an average weight of 3 mg. CR2025 coin cells were assembled in a glovebox filled with pure argon gas ( $\text{O}_2$  and  $\text{H}_2\text{O}$  content < 1 ppm), using lithium pellets as the anode and a 1 M solution of  $\text{LiPF}_6$  in ethylene carbon/dimethyl carbonate as the electrolyte. Before the charging/discharging process, the cells were aged for 12 h to ensure full absorption of the electrolyte into the electrodes. The electrode area was  $0.636 \text{ cm}^2$  (the disk with a diameter of 9 mm), and the mass loading was  $4.72 \text{ mg cm}^{-2}$  (3 mg in  $0.636 \text{ cm}^2$ ). Galvanostatic charging/discharging tests were performed in the voltage range of 2.5–4.5 V at different current densities on a multichannel battery testing system (LAND CT2001A). The cells were charged under a constant current and constant voltage mode, which was then discharged under a constant current mode. The constant current charging is followed by a potentiostatic holding at 4.5 V until the current drops to 5% of the original charging current. The cells were then discharged to 2.5 V. A cyclic voltammetry (CV) test of the cells was carried out with an electrochemical workstation (CHI 760D). The electrochemical impedance spectroscopy (EIS) was tested using another electrochemical workstation (Autolab PGSTAT 302N) at a cell voltage of 4.4 V in the frequency range of 100 kHz to 0.01 Hz with the amplitude of 10 mV. All of the tests were performed at room temperature.

### 3. RESULTS AND DISCUSSION

The XRD patterns in Figure 1A show that the prepared LMP·LVP-1 can be indexed to  $\text{LiMnPO}_4$  with an orthorhombic structure [JCPDS 00-033-0804; space group of  $Pmnb$  (No. 62)], which is consistent with previous reports.<sup>26,27</sup> However, diffraction peaks from the impurity,  $\text{Mn}_2\text{P}_2\text{O}_7$  with a monoclinic structure (JCPDS 00-029-0891), can also be detected, which may result from the initial reaction between  $(\text{CH}_3\text{COO})_2\text{Mn}\cdot 4\text{H}_2\text{O}$  and  $\text{H}_3\text{PO}_4$ . While LMP·LVP-2 to LMP·LVP-5 are the composites of  $\text{LiMnPO}_4$  (JCPDS 00-033-0804) and  $\text{Li}_3\text{V}_2(\text{PO}_4)_3$  (JCPDS 00-072-7074) without other impurities, the relative peak intensities are consistent with the corresponding ratios of  $\text{LiMnPO}_4$  to  $\text{Li}_3\text{V}_2(\text{PO}_4)_3$ . It is worth noting that there is no graphitic carbon diffraction peak in the XRD patterns. The Raman spectrum of LMP·LVP-3 displays two characteristic bands of carbonaceous materials located at  $1348\text{ cm}^{-1}$  (D band, disorder-induced phonon mode) and  $1594\text{ cm}^{-1}$  (G band,  $\text{E}_{2g}$  vibration of graphite) (Figure 1B).<sup>28</sup> The  $I_D/I_G$  value is 0.75, indicating the highly graphitic nature of carbon with improved electronic conductivity.<sup>20</sup> The highly graphitized carbon could be attributed to the existence of manganese, as manganese could act as a graphitization catalyst for preparing graphitic carbon nanostructures at moderate temperatures ( $<1000\text{ }^\circ\text{C}$ ). As a result, the graphitization degree of the carbons increases greatly even at low temperature.<sup>29,30</sup> However, the highly graphitized carbon may be very small in size without a long-range order. As a result, it is difficult to detect any graphite crystallites from XRD.<sup>31</sup>

The typical Rietveld refinement XRD patterns of LMP·LVP are shown as Figure 1C–F, and the corresponding refined results are shown in Table S1. It is clear that the cell volume of LMP in the LMP·LVP composites gradually reduces with the increased ratio of LVP. According to the XRD results, LMP and LVP coexist in the final composite, in which  $\text{V}^{3+}$  could dope on the  $\text{Mn}^{2+}$  sites during the crystal growth process. The smaller ionic radius of  $\text{V}^{3+}$  (0.74 Å) compared to that of  $\text{Mn}^{2+}$  (0.80 Å) results in the cell volume reduction.<sup>5,15,16</sup> As a result, the electronic conductivity of LMP would be improved with the doping of  $\text{V}^{3+}$ , enabling the sufficient utilization of LMP in the composite.<sup>32,33</sup>

The morphology of LMP·LVP-3 observed with FESEM is shown in Figure 2A,C, indicating that LMP·LVP-3 possesses a highly porous structure, in which the primary particles are well-embedded in the carbon matrix. Energy-dispersive X-ray spectroscopy results of LMP·LVP-3 show that the manganese, vanadium, phosphorus, and carbon are distributed uniformly in the final product (Figure 2B).

The porous structure of LMP·LVP-3 is further confirmed by TEM and HRTEM images (Figure 2D–G). It is clearly observed that LMP·LVP-3 is porous with voids between nanoparticles. Furthermore, the primary nanoparticles with sizes around 100 nm are uniformly embedded in the carbon matrix (Figure 2D). In the HRTEM images, LMP exhibits higher contrast and the dark LMP particle shows a typical morphology of olivine, and the surrounding LVP nanoparticles show lattice spacings of 0.27 and 0.30 nm, corresponding to the (102) and (022) planes of monoclinic  $\text{Li}_3\text{V}_2(\text{PO}_4)_3$ , respectively (Figure 2E). LVP can act as the lithium-ion transportation media for LMP, which is beneficial for the utilization of LMP active material. Another zone shows the clear boundary between the LMP and LVP nanoparticles, and the lattice fringes from both components can be seen (Figure 2F). The

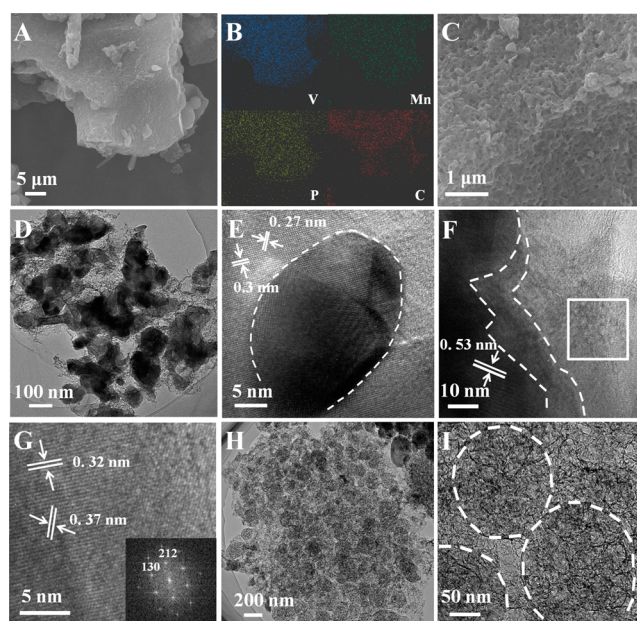


**Figure 2.** (A–C) SEM and element mapping images of LMP·LVP-3. (D–G) TEM and HRTEM images of LMP·LVP-3. (H and I) TEM images of the pure carbon network.

left part of the particle displays a clear crystal lattice spacing of 0.53 nm, which matches well with the (020) plane of orthorhombic  $\text{LiMnPO}_4$ . The square area in Figure 2F is further enlarged in Figure 2G. And two obvious crystal lattice spacings of 0.32 and 0.37 nm can be clearly observed, which match well with the (212) and (130) planes of monoclinic  $\text{Li}_3\text{V}_2(\text{PO}_4)_3$ , respectively. In the zone between the two white dashed lines, the two phases probably coexist.

In order to explore the characteristics of the carbon matrix, the pure carbon network was obtained via etching LMP·LVP-3 in a hydrofluoric acid solution (Figure 2H,I). The resultant carbon matrix exhibits a 3D continuous carbon network, indicating that the carbon is not only coating the surface of the primary particles but also connecting the particles together to form a continuous electron-transport network. After etching off the active materials, some cavities can be observed in the carbon network (marked by dashed lines in Figure 2I), indicating that the active materials are well-wrapped by the carbon matrix.

The LMP/LVP ratio has a great influence on the morphology of the final products. For LMP·LVP-1, the primary particles are generally larger than  $1\text{ }\mu\text{m}$  and irregular in shape. The micron-sized irregular particles stack with each other into larger secondary particles without obvious pores (Figure S2A). This could be attributed to the direct reaction between  $(\text{CH}_3\text{COO})_2\text{Mn}\cdot 4\text{H}_2\text{O}$  and  $\text{H}_3\text{PO}_4$ . Actually, white precipitates ( $\text{H}_{10}\text{Mn}_5\text{O}_{20}\text{P}_4$ ; JCPDS 00-078-1648) appear immediately after the addition of  $\text{H}_3\text{PO}_4$  into a  $(\text{CH}_3\text{COO})_2\text{Mn}\cdot 4\text{H}_2\text{O}$  solution (Figure S3A–C). For LMP·LVP-2 with 20% LVP, a blue solution with yellow precipitates are obtained before drying. The morphology of the yellow precipitates is uniform, and the particle size is around 200–500 nm (Figure S3D,E). Different from the white precipitates, the yellow precipitates are amorphous without any XRD peaks (Figure S3F). For both LMP·LVP-1 and LMP·LVP-2, the carbon simply coats the surface of the primary particles, which cannot prevent the particles from agglomeration. For LMP·LVP-3, LMP·LVP-4,

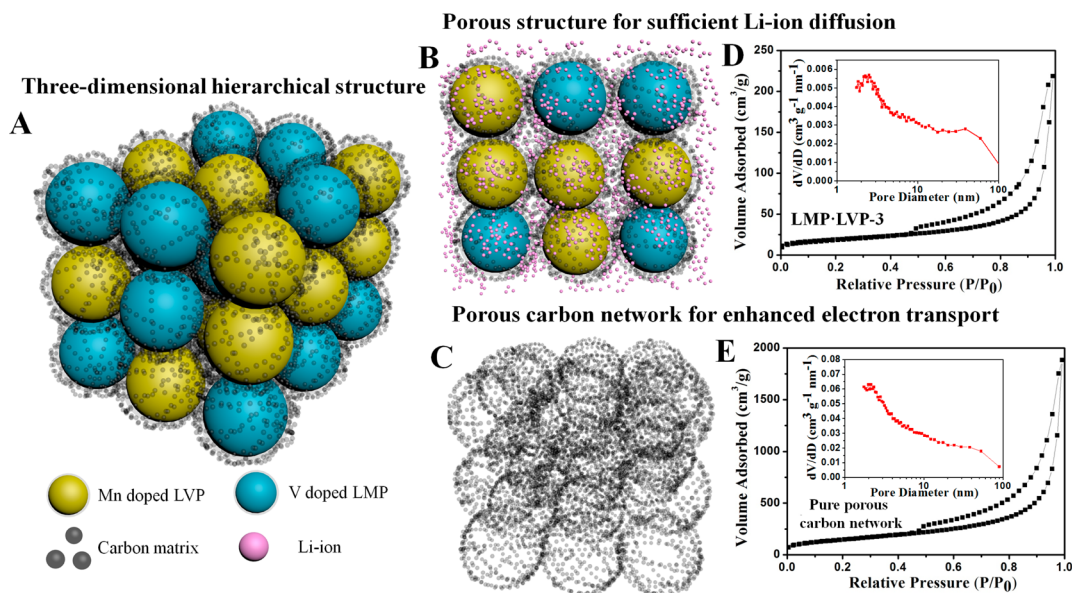


**Figure 3.** (A–C) Schematic illustrations of the hierarchical carbon-decorated LMP-LVP-3 and pure porous carbon network with pathways for both electrons and lithium ions. (D and E) Nitrogen adsorption–desorption isotherms of LMP-LVP-3 and a pure porous carbon network after etching off the LMP-LVP-3 particles, respectively. The insets show the corresponding BJH pore-size distribution curves.

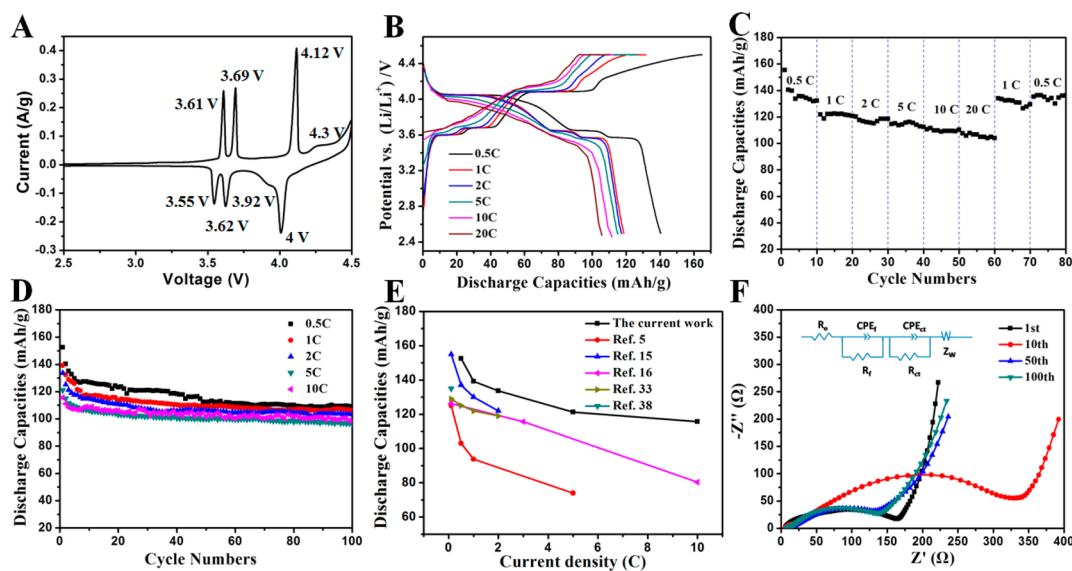


**Figure 4.** Electrochemical properties of LMP-LVP-3. (A) CV curves at a sweep rate of  $0.1 \text{ mV s}^{-1}$  in the potential range from 2.5 to 4.5 V vs  $\text{Li/Li}^+$ . (B) Second charge/discharge curves of LMP-LVP-3 at the current densities of 0.5, 1, 2, 5, 10, and 20 C. (C) Rate performance of LMP-LVP-3 at various rates from 0.5 to 20 C. (D) Detailed cycling performance of LMP-LVP-3 at different rates. (E) Comparison of the electrochemical performances between this work and previous reports on vanadium-doped  $\text{LiMnPO}_4$ . (F) Typical Nyquist plots of LMP-LVP-3 after different cycles.

and LMP-LVP-5, a transparent solution without any precipitates is always obtained, indicating the uniform dispersion of the reactive ions in the solution. Moreover, these three samples have similar porous morphologies with carbon bridging the neighboring particles (Figures 2A and S2C,D). Also, according to the elemental analysis results, the amounts of carbon in LMP-LVP-1 to LMP-LVP-5 are about 7.8%, 7.2%, 5.0%, 4.7%, and 4.2%, respectively. The result is consistent with the composition because glucose can act as the reducing agent to reduce  $\text{VOCl}_2$  in the synthesis process. However, the value of LMP-LVP-3 is still a little higher than those of other reports on  $\text{LiMnPO}_4$ , which could be attributed to the coexistence of the protective carbon coating and hierarchical carbon bridges between the primary particles.<sup>16,20</sup>

Parts A–C of Figure 3 display the schematic of the 3D LMP-LVP/C nanocomposite, in which the active nanoparticles are well-embedded in a conductive carbon network (Figure 3A). The architecture of this hierarchical carbon-decorated (carbon network and surface carbon coating) LMP-LVP could simultaneously provide the rapid ion transport enabled by an electrolyte-filled porous network and continuous electron conduction enabled by hierarchical carbon (Figure 3B,C).<sup>34</sup> Nitrogen sorption is also conducted to gain information on the porous properties of the samples (Figures 3D and S4), and the Brunauer–Emmett–Teller (BET) surface areas and total pore volumes of the samples are listed in Table S2. Generally, the BET surface area increases with increasing LVP percentage. Because no pores can be observed in the SEM images, the

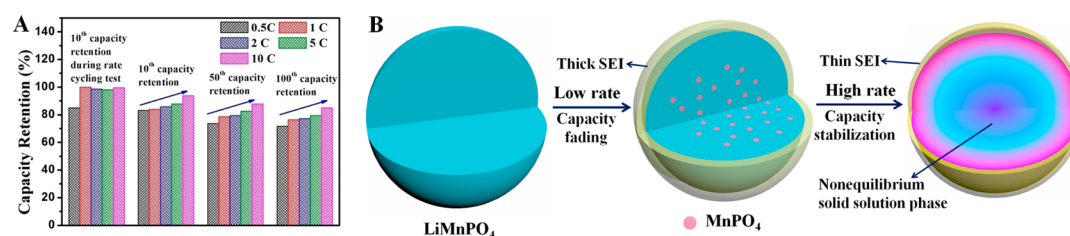


**Figure 5.** (A) Comparison of the capacity retentions at different rates. (B) Proposed model for the phase transitions of LMP-LVP-3 at high and low rates.

surface areas of LMP-LVP-1 and LMP-LVP-2 should be contributed from the surface carbon coating. Among the five samples, LMP-LVP-3 possesses a surface area of  $68.3 \text{ m}^2 \text{ g}^{-1}$  and the highest pore volume of  $0.331 \text{ cm}^3 \text{ g}^{-1}$ , which may facilitate electrolyte penetration and thus improve the ionic diffusion rate. After the HF etching, a high surface area of  $522 \text{ m}^2 \text{ g}^{-1}$  is obtained for this 3D carbon network using nitrogen sorption (Figure 3E). LMP-LVP-4 and LMP-LVP-5 show a porous structure similar to that of LMP-LVP-3 with even higher surface area. The cycling performances of LMP-LVP with different compositions are shown in Figure S5. LMP-LVP-3 to LMP-LVP-5 show similar electrochemical performances, which are much better than those of LMP-LVP-1 and LMP-LVP-2. The better performance of vanadium-rich samples (LMP-LVP-3 to LMP-LVP-5) can be attributed to the higher ionic conductivity of  $\text{Li}_3\text{V}_2(\text{PO}_4)_3$  ( $10^{-9}$ – $10^{-10} \text{ cm}^2 \text{ s}^{-1}$ ) than that of  $\text{LiMnPO}_4$  ( $\sim 10^{-15} \text{ cm}^2 \text{ s}^{-1}$ ). Considering the lower cost and toxicity of manganese compared to vanadium, LMP-LVP-3 is considered as the optimized composite for lithium-ion battery application and is mainly investigated in this work.

Figure 4A shows the first cycle CV curve of LMP-LVP-3 at a scan rate of  $0.1 \text{ mV s}^{-1}$  between 2.5 and 4.5 V vs Li/Li<sup>+</sup>. During the charge process, four well-defined oxidation peaks are observed at 3.61, 3.69, 4.12, and 4.30 V (vs Li/Li<sup>+</sup>), respectively. The peaks at 3.61 and 3.69 V are associated with the phase transitions of  $\text{Li}_3\text{V}_2(\text{PO}_4)_3$  to  $\text{Li}_{2.5}\text{V}_3(\text{PO}_4)_3$  (eq 1) and  $\text{Li}_{2.5}\text{V}_3(\text{PO}_4)_3$  to  $\text{Li}_2\text{V}_3(\text{PO}_4)_3$  (eq 2), respectively. The peak located at 4.12 V is related to delithiation of the second lithium ion to form  $\text{LiV}_2(\text{PO}_4)_3$  (eq 3).<sup>35,36</sup> The reduction peaks at 3.55, 3.62, and 4.00 V in the subsequent discharge process are ascribed to the reversible insertion of extracted lithium ions in  $\text{Li}_3\text{V}_2(\text{PO}_4)_3$ . The redox peaks at 3.92 and 4.30 V are associated with the reduction and oxidation of the  $\text{Mn}^{2+}/\text{Mn}^{3+}$  redox couple (eq 4), respectively.<sup>5,37</sup> It is worth noting that the redox peaks for  $\text{Li}_3\text{V}_2(\text{PO}_4)_3$  are very strong and sharp, while the redox peaks for  $\text{LiMnPO}_4$  are very weak and broad. This phenomenon could be attributed to the much higher ionic conductivity of  $\text{Li}_3\text{V}_2(\text{PO}_4)_3$  ( $10^{-9}$ – $10^{-10} \text{ cm}^2 \text{ s}^{-1}$ ) than that of  $\text{LiMnPO}_4$  ( $\sim 10^{-15} \text{ cm}^2 \text{ s}^{-1}$ ) because a higher redox peak current corresponds to faster kinetics for lithium-ion insertion/extraction.<sup>3</sup>

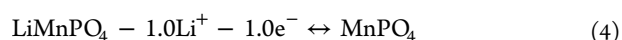
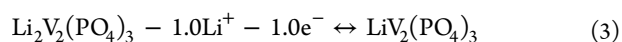
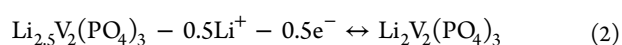
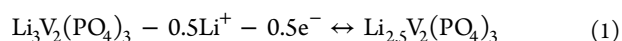


Figure 4B exhibits the second charge/discharge curves of LMP-LVP-3 at the current densities of 0.5, 1, 2, 5, 10, and 20 C

(1 C =  $170 \text{ mA g}^{-1}$ ). The locations of the plateaus are consistent with the CV results. With increased charge/discharge current density, the plateaus become shorter and less distinct, and the polarization would become more serious. However, the plateaus of LMP-LVP-3 are still apparent even under the high current rate of 20 C, which is attributed to the porous structure and high conductivity of the hierarchical carbon-decorated cathode material.

The rate performance of LMP-LVP-3 is shown in Figure 4C. It is clear that LMP-LVP-3 exhibits a reasonably good cycling response at various current rates. When cycled at 0.5, 1, 2, 5, and 10 C, it delivers capacities of 155, 122, 120, 115, and 111  $\text{mA h g}^{-1}$ , respectively. Remarkably, even after 50 cycles, the electrode still obtains a capacity of  $108 \text{ mA h g}^{-1}$  at a current density of 20 C. After the high rate measurement, LMP-LVP-3 is able to supply a high capacity of  $134 \text{ mA h g}^{-1}$  when the current is reduced to 1 C again. This value is even higher than that delivered before the high rate test at 1 C. The rate performance highly manifests the excellent structural stability and the resulting high reversibility of LMP-LVP-3, which should be attributed to the rationally designed 3D bicontinuous nanostructure. The detailed cycling performance of LMP-LVP-3 at different rates is displayed in Figure 4D. It delivers high initial capacities of 153, 139, 134, 121, and  $116 \text{ mA h g}^{-1}$  under current densities of 0.1, 1, 2, 5, and 10 C, respectively. To the best of our knowledge, the electrochemical performance of this 3D hierarchical LMP-LVP-3 cathode material is superior to the vanadium-doped  $\text{LiMnPO}_4$  electrode materials reported recently (Figure 4E).<sup>5,15,16,33,38</sup>

The EIS results of LMP-LVP-3 during cycling were collected in the frequency range 100 kHz to 0.01 Hz at a voltage of 4.4 V (Figure 4F). All of the Nyquist plots are composed of a small intercept in the highest frequency and two depressed semicircles at high and middle frequencies, combined with a slanted line in the low frequency region. The arc centered at high frequency can be attributed to the resistance caused by the formation of a solid-electrolyte interphase (SEI) layer ( $R_f$ ) and the double-layer capacitance caused by the conductive substrate and electrolyte ( $\text{CPE}_f$ ), while the latter arc indicates the charge-transfer resistance ( $R_{ct}$ ) combined with the double-layer capacitance ( $\text{CPE}_{ct}$ ) between the active material and electrolyte. The slanted line corresponds to the ion diffusion ( $Z_W$ ) in the active material.<sup>39</sup> After 10 cycles of galvanostatic charge/discharge,  $R_{ct}$  increases dramatically from 138 to  $331 \Omega$ , which is associated with the formation of a thick SEI, the slight dissolution of the active material, and side reactions.<sup>40</sup> As a result, the capacity decrease during cycling is obvious in the initial 10 cycles. However, after 50 cycles, the EIS plots show a decreased  $R_{ct}$  ( $113 \Omega$ ) as the SEI gradually becomes thin, uniform, and stable, which is beneficial for lithium-ion transport. This speculation is confirmed by the EIS plot after

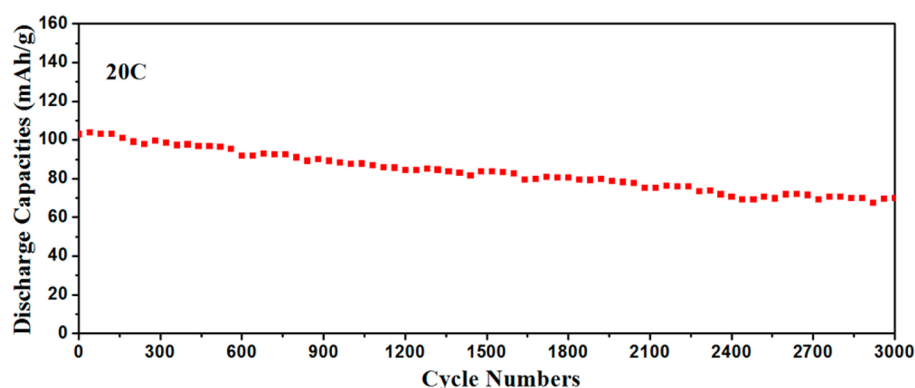


Figure 6. Electrochemical properties of LMP-LVP-3 at a high rate of 20 C for 3000 cycles.

100 cycles, which shows a feature similar to that of the electrode after 50 cycles, indicating the good electrode stability during the cycling process.

The capacity retentions at the 10th, 50th, and 100th cycles under different current densities are compared and show an interesting phenomenon. No matter what the current is, the capacity retention increases gradually along with the increasing current density (specific data are recorded in Table S3). However, the retentions during the rate performance test do not follow the above trend. More importantly, the retentions during the rate performance test are much higher than those in the cycling performance tests (Figure 5A). Because the lithium-ion diffusion rate in  $\text{Li}_3\text{V}_2(\text{PO}_4)_3$  is relatively higher than that in  $\text{LiMnPO}_4$ , the capacity decay is mainly attributed to the destruction of  $\text{LiMnPO}_4$ . The crystal structures and electrochemical reactions of  $\text{LiMnPO}_4$  and  $\text{LiFePO}_4$  are similar, which indicates that the investigations on  $\text{LiFePO}_4$  would provide guidance to  $\text{LiMnPO}_4$ . It is reported that the (dis)charge rates would have a great impact on the phase transition mechanism in the olivine system.<sup>41–43</sup> A phase transformation is induced as a result of the lithium compositional changes within an electrode at low rates, while a nonequilibrium solid solution can be formed during the electrochemical reaction to bypass the nucleation step at high rates.<sup>41</sup> Thus, it is hypothesized that the phase transition in  $\text{LiMnPO}_4$  at low rates is processed via a distinct moving phase boundary between  $\text{LiMnPO}_4$  and  $\text{MnPO}_4$  with major structural rearrangement. In contrast,  $\text{LiMnPO}_4$  would transform via a moving nonequilibrium single solid–solution phase with a continuous change in the composition rather than a significant structural change at high rates. As a consequence, the capacity retention would increase with an increase of the current density. Meanwhile, the primary capacity decay takes place within the initial 10 cycles, which is mainly due to structural degradation and unstable SEI formation upon cycling. The high mechanical stress induced by repetitive volume expansion/contraction of  $\text{LiMnPO}_4$  at low rates would exfoliate and reform a thick SEI. When high-rate lithiation is applied, the formation of nonequilibrium solid solution phase could effectively reduce the volume expansion and mitigate stress impaction, which means that a thin and stable SEI can be formed without fracture (Figure 5B).<sup>44</sup> It is speculated that if the active material is first activated at low rates to take full advantage of materials and then a high rate is applied to induce the thin and stable SEI layer, and improved Coulombic efficiency, exceptional rate capability, and extended lifetime would be realized.

Figure 6 displays the long-life performance of the LMP-LVP-3 cathode at a current density of 20 C. On the basis of the above discussions, the battery was activated at 0.5 C for 10 cycles for a better electrochemical performance. When discharged at 20 C, the battery displays a relatively high capacity of  $103 \text{ mA h g}^{-1}$ . The specific capacity decreased to  $70 \text{ mA h g}^{-1}$  after 3000 cycles, corresponding to a capacity retention of 68% and a capacity fading of 0.013% per cycle. The excellent electrochemical performance indicates that LMP-LVP-3 is a promising candidate as a high-rate and long-life cathode material for lithium-ion batteries.

#### 4. CONCLUSION

In summary, a 3D hierarchical carbon-decorated LMP-LVP nanocomposite was designed with the active nanoparticles well-embedded in a conductive carbon network. A high surface area of  $68.3 \text{ m}^2 \text{ g}^{-1}$  and a high pore volume of  $0.331 \text{ cm}^3 \text{ g}^{-1}$  can be obtained, providing efficient pores for the penetration of lithium ions. When cycled at 20 C, a high specific capacity of  $103 \text{ mA h g}^{-1}$  can be obtained. Even after 3000 cycles, the capacity retention is still up to 68%, corresponding to a capacity fading of 0.013% per cycle. This outstanding high-rate performance and excellent cyclic stability may be attributed to the uniquely designed architecture. Our work indicates that this hierarchical carbon-decorated LMP-LVP is one of the most attractive cathodes for practical applications. In view of the facility during synthesis, the synthetic strategy could also be extended to other cathode and anode materials.

#### ■ ASSOCIATED CONTENT

##### Supporting Information

The Supporting Information is available free of charge on the ACS Publications website at DOI: 10.1021/acsami.5b05451.

Synthesis process of  $n\text{LiMnPO}_4 \cdot (1 - n)\text{Li}_3\text{V}_2(\text{PO}_4)_3$  samples and the influence of different molar ratios on the phase and morphology of the products, investigated by XRD, SEM, and BET (PDF)

#### ■ AUTHOR INFORMATION

##### Corresponding Author

\*E-mail: mlq518@whut.edu.cn.

##### Author Contributions

The manuscript was written through contributions of all authors. All authors have given approval to the final version of the manuscript.

## Notes

The authors declare no competing financial interest.

## ACKNOWLEDGMENTS

This work was supported by the National Basic Research Program of China (Grants 2013CB934103 and 2012CB933003), the International Science & Technology Cooperation Program of China (Grant 2013DFA50840), and National Natural Science Foundation of China (Grants 51072153 and 51272197). Thanks go to Prof. C. M. Lieber of Harvard University and Prof. Dongyuan Zhao of Fudan University for strong support and stimulating discussion.

## REFERENCES

- Xie, Y.; Yu, H. T.; Yi, T. F.; Zhu, Y. R. Understanding the Thermal and Mechanical Stabilities of Olivine-Type  $\text{LiMPO}_4$  ( $M = \text{Fe}, \text{Mn}$ ) as Cathode Materials for Rechargeable Lithium Batteries from First Principles. *ACS Appl. Mater. Interfaces* **2014**, *6*, 4033–4042.
- Ding, B.; Xiao, P. F.; Ji, G.; Ma, Y.; Lu, L.; Lee, J. Y. High-Performance Lithium-Ion Cathode  $\text{LiMn}_{0.7}\text{Fe}_{0.3}\text{PO}_4/\text{C}$  and the Mechanism of Performance Enhancements through Fe Substitution. *ACS Appl. Mater. Interfaces* **2013**, *5*, 12120–12126.
- Hu, L. J.; Qiu, B.; Xia, Y. G.; Qin, Z. H.; Qin, L. F.; Zhou, X. F.; Liu, Z. P. Solvothermal Synthesis of Fe-Doping  $\text{LiMnPO}_4$  Nanomaterials for Li-Ion Batteries. *J. Power Sources* **2014**, *248*, 246–252.
- Liu, S.; Fang, H. S.; Yang, B.; Yao, Y. C.; Ma, W. H.; Dai, Y. N. Improving Rate Performance of  $\text{LiMnPO}_4$  Based Material by Forming Electron-Conducting Iron Phosphides. *J. Power Sources* **2013**, *230*, 267–270.
- Qin, L. F.; Xia, Y. G.; Qiu, B.; Cao, H. L.; Liu, Y. Z.; Liu, Z. P. Synthesis and Electrochemical Performances of  $(1-x)\text{LiMnPO}_4 \cdot x\text{Li}_3\text{V}_2(\text{PO}_4)_3/\text{C}$  Composite Cathode Materials for Lithium Ion Batteries. *J. Power Sources* **2013**, *239*, 144–150.
- Cui, Y. T.; Xu, N.; Kou, L. Q.; Wu, M. T.; Chen, L. Enhanced Electrochemical Performance of Different Morphological  $\text{C}/\text{LiMnPO}_4$  Nanoparticles from Hollow-Sphere  $\text{Li}_3\text{PO}_4$  Precursor via a Delicate Polyol-Assisted Hydrothermal Method. *J. Power Sources* **2014**, *249*, 42–47.
- Zhu, H. J.; Zhai, W.; Yang, M.; Liu, X. M.; Chen, Y. C.; Yang, H.; Shen, X. D. Synthesis and Characterization of  $\text{LiMnPO}_4/\text{C}$  Nanocomposites from Manganese(II) Phosphate Trihydrate Precipitated from a Micro-Channel Reactor Approach. *RSC Adv.* **2014**, *4*, 25625–25632.
- Dai, Z. J.; Wang, L.; Ye, F. P.; Huang, C. C.; Wang, J. X.; Huang, X. K.; Wang, J. L.; Tian, G. Y.; He, X. M.; Ouyang, M. G. Influence of Anion Species on the Morphology of Solvothermal Synthesized  $\text{LiMn}_{0.9}\text{Fe}_{0.1}\text{PO}_4$ . *Electrochim. Acta* **2014**, *134*, 13–17.
- Milke, B.; Strauch, P.; Antonietti, M.; Giordano, C. Synthesis of  $\text{Li}_y\text{MnSiO}_x$  and  $\text{LiMnPO}_4$  Nanostructures. *Nanoscale* **2009**, *1*, 110–113.
- Kwon, N. H.; Fromm, K. M. Enhanced Electrochemical Performance of  $< 30$  nm Thin  $\text{LiMnPO}_4$  Nanorods with a Reduced Amount of Carbon as a Cathode for Lithium Ion Batteries. *Electrochim. Acta* **2012**, *69*, 38–44.
- Qin, L. F.; Xia, Y. G.; Cao, H. L.; Luo, L. J.; Zhang, Q.; Chen, L. P.; Liu, Z. P. Effects of Ti Additive on the Structure and Electrochemical Performance of  $\text{LiMnPO}_4$  Cathode Material. *Electrochim. Acta* **2014**, *123*, 240–247.
- Pivko, M.; Bele, M.; Tchernychova, E.; Logar, N. Z.; Dominko, R.; Gaberscek, M. Synthesis of Nanometric  $\text{LiMnPO}_4$  via a Two-Step Technique. *Chem. Mater.* **2012**, *24*, 1041–1047.
- Damen, L.; De Giorgio, F.; Monaco, S.; Veronesi, F.; Mastragostino, M. Synthesis and Characterization of Carbon-Coated  $\text{LiMnPO}_4$  and  $\text{LiMn}_{1-x}\text{Fe}_x\text{PO}_4$  ( $x = 0.2, 0.3$ ) Materials for Lithium-Ion Batteries. *J. Power Sources* **2012**, *218*, 250–253.
- Dinh, H. C.; Mho, S. I.; Kang, Y.; Yeo, I. H. Large Discharge Capacities at High Current Rates for Carbon-Coated  $\text{LiMnPO}_4$  Nanocrystalline Cathodes. *J. Power Sources* **2013**, *244*, 189–195.
- Wang, F.; Yang, J.; NuLi, Y. N.; Wang, J. L. Composites of  $\text{LiMnPO}_4$  with  $\text{Li}_3\text{V}_2(\text{PO}_4)_3$  for Cathode in Lithium-Ion Battery. *Electrochim. Acta* **2013**, *103*, 96–102.
- Zhang, B.; Wang, X. W.; Zhang, J. F. Novel Synthesis of  $\text{LiMnPO}_4 \cdot \text{Li}_3\text{V}_2(\text{PO}_4)_3/\text{C}$  Composite Cathode Material. *RSC Adv.* **2014**, *4*, 49123–49127.
- Sun, C. W.; Rajasekhara, S.; Dong, Y. Z.; Goodenough, J. B. Hydrothermal Synthesis and Electrochemical Properties of  $\text{Li}_3\text{V}_2(\text{PO}_4)_3/\text{C}$ -Based Composites for Lithium-Ion Batteries. *ACS Appl. Mater. Interfaces* **2011**, *3*, 3772–3776.
- Li, D. L.; Tian, M.; Xie, R.; Li, Q.; Fan, X. Y.; Gou, L.; Zhao, P.; Ma, S. L.; Shi, Y. X.; Yong, H. T. H. Three-Dimensionally Ordered Macroporous  $\text{Li}_3\text{V}_2(\text{PO}_4)_3/\text{C}$  Nanocomposite Cathode Material for High-Capacity and High-Rate Li-Ion Batteries. *Nanoscale* **2014**, *6*, 3302–3308.
- Wang, J. X.; Wang, Z. X.; Li, X. H.; Guo, H. J.; Wu, X. W.; Zhang, X. P.; Xiao, W.  $x\text{Li}_3\text{V}_2(\text{PO}_4)_3/\text{LiVPO}_4\text{F}/\text{C}$  Composite Cathode Materials for Lithium Ion Batteries. *Electrochim. Acta* **2013**, *87*, 224–229.
- Luo, Y. Z.; Xu, X.; Zhang, Y. X.; Pi, Y. Q.; Zhao, Y. L.; Tian, X. C.; An, Q. Y.; Wei, Q. L.; Mai, L. Q. Hierarchical Carbon Decorated  $\text{Li}_3\text{V}_2(\text{PO}_4)_3$  as a Bicontinuous Cathode with High-Rate Capability and Broad Temperature Adaptability. *Adv. Energy Mater.* **2014**, *4*, 1400107.
- Fang, Y.; Zheng, G. F.; Yang, J. P.; Tang, H. S.; Zhang, Y. F.; Kong, B.; Lv, Y. Y.; Xu, C. J.; Asiri, A. M.; Zi, J.; Zhang, F.; Zhao, D. Y. Dual-Pore Mesoporous Carbon@Silica Composite Core-Shell Nanospheres for Multidrug Delivery. *Angew. Chem., Int. Ed.* **2014**, *53*, 5366–5370.
- Oh, S. M.; Oh, S. W.; Yoon, C. S.; Scrosati, B.; Amine, K.; Sun, Y. K. High-Performance Carbon- $\text{LiMnPO}_4$  Nanocomposite Cathode for Lithium Batteries. *Adv. Funct. Mater.* **2010**, *20*, 3260–3265.
- Yoo, H.; Jo, M.; Jin, B. S.; Kim, H. S.; Cho, J. Flexible Morphology Design of 3D-Macroporous  $\text{LiMnPO}_4$  Cathode Materials for Li Secondary Batteries: Ball to Flake. *Adv. Energy Mater.* **2011**, *1*, 347–351.
- Raju, V.; Rains, J.; Gates, C.; Luo, W.; Wang, X. F.; Stickle, W. F.; Stucky, G. D.; Ji, X. L. Superior Cathode of Sodium-Ion Batteries: Orthorhombic  $\text{V}_2\text{O}_5$  Nanoparticles Generated in Nanoporous Carbon by Ambient Hydrolysis Deposition. *Nano Lett.* **2014**, *14*, 4119–4124.
- Li, L.; Wang, H. Q.; Fang, X. S.; Zhai, T. Y.; Bando, Y.; Golberg, D. High-Performance Schottky Solar Cells using  $\text{ZrS}_2$  Nanobelt Networks. *Energy Environ. Sci.* **2011**, *4*, 2586–2590.
- Zhao, M.; Fu, Y.; Xu, N.; Li, G. R.; Wu, M. T.; Gao, X. P. High Performance  $\text{LiMnPO}_4/\text{C}$  Prepared by a Crystallite Size Control Method. *J. Mater. Chem. A* **2014**, *2*, 15070–15077.
- Ran, L. B.; Liu, X. Y.; Tang, Q. W.; Zhu, K. L.; Tian, J. H.; Du, J. Y.; Shan, Z. Q. Grinding Aid-Assisted Preparation of High-Performance Carbon- $\text{LiMnPO}_4$ . *Electrochim. Acta* **2013**, *114*, 14–20.
- Rui, X. H.; Sim, D. H.; Wong, K. M.; Zhu, J. X.; Liu, W. L.; Xu, C.; Tan, H. T.; Xiao, N.; Hng, H. H.; Lim, T. M.; Yan, Q. Y.  $\text{Li}_3\text{V}_2(\text{PO}_4)_3$  Nanocrystals Embedded in a Nanoporous Carbon Matrix Supported on Reduced Graphene Oxide Sheets: Binder-Free and High Rate Cathode Material for Lithium-Ion Batteries. *J. Power Sources* **2012**, *214*, 171–177.
- Sevilla, M.; Fuertes, A. B. Catalytic graphitization of templated mesoporous carbons. *Carbon* **2006**, *44*, 468–474.
- Sevilla, M.; Sanchis, C.; Valdés-Solis, T.; Morallón, E.; Fuertes, A. B. Direct synthesis of graphitic carbon nanostructures from saccharides and their use as electrocatalytic supports. *Carbon* **2008**, *46*, 931–939.
- Chen, Y. S.; Zhang, D. X.; Bian, F.; Bie, X. F.; Wang, C. Z.; Du, F.; Jang, M.; Chen, G.; Wei, Y. J. Characterizations of the Electrode/Electrolyte Interfacial Properties of Carbon Coated  $\text{Li}_3\text{V}_2(\text{PO}_4)_3$  Cathode Material in  $\text{LiPF}_6$  Based Electrolyte. *Electrochim. Acta* **2012**, *79*, 95–101.

- (32) Chen, L.; Yan, B.; Xie, Y. F.; Wang, S. M.; Jiang, X. F.; Yang, G. Preparation and Electrochemical Properties of  $\text{Li}_3\text{V}_{1.8}\text{Mn}_{0.2}(\text{PO}_4)_3$  Doped via Different Mn Sources. *J. Power Sources* **2014**, *261*, 188–197.
- (33) Wang, C. Y.; Bi, Y. J.; Liu, Y.; Qin, Y. P.; Fang, Y. Q.; Wang, D. Y. Investigation of  $(1-x)\text{LiMnPO}_4 \cdot x\text{Li}_3\text{V}_2(\text{PO}_4)_3/\text{C}$ : Phase Composition and Electrochemical Performance. *J. Power Sources* **2014**, *263*, 332–337.
- (34) Wu, X. L.; Jiang, L. Y.; Cao, F. F.; Guo, Y. G.; Wan, L. J.  $\text{LiFePO}_4$  Nanoparticles Embedded in a Nanoporous Carbon Matrix: Superior Cathode Material for Electrochemical Energy-Storage Devices. *Adv. Mater.* **2009**, *21*, 2710–2714.
- (35) Zhang, L. L.; Liang, G.; Peng, G.; Zou, F.; Huang, Y. H.; Croft, M. C.; Ignatov, A. Significantly Improved Electrochemical Performance in  $\text{Li}_3\text{V}_2(\text{PO}_4)_3/\text{C}$  Promoted by  $\text{SiO}_2$  Coating for Lithium-Ion Batteries. *J. Phys. Chem. C* **2012**, *116*, 12401–12408.
- (36) Yuan, W.; Yan, J.; Tang, Z. Y.; Sha, O.; Wang, J. M.; Mao, W. F.; Ma, L. Synthesis of  $\text{Li}_3\text{V}_2(\text{PO}_4)_3$  Cathode Material via a Fast Sol-Gel Method Based on Spontaneous Chemical Reactions. *J. Power Sources* **2012**, *201*, 301–306.
- (37) Su, K.; Liu, F.; Chen, J. T. Preparation of High Performance Carbon-Coated  $\text{LiMnPO}_4$  Nanocomposite by an Acetate-Assisted Antisolvent Precipitation Method. *J. Power Sources* **2013**, *232*, 234–239.
- (38) Su, L.; Li, X.; Ming, H.; Adkins, J.; Liu, M.; Zhou, Q.; Zheng, J. Effect of Vanadium Doping on Electrochemical Performance of  $\text{LiMnPO}_4$  for Lithium-Ion Batteries. *J. Solid State Electrochem.* **2014**, *18*, 755–762.
- (39) Ji, H. X.; Zhang, L. L.; Pettes, M. T.; Li, H. F.; Chen, S. S.; Shi, L.; Piner, R.; Ruoff, R. S. Ultrathin Graphite Foam: A Three-Dimensional Conductive Network for Battery Electrodes. *Nano Lett.* **2012**, *12*, 2446–2451.
- (40) Jia, X. L.; Chen, Z.; Cui, X.; Peng, Y. T.; Wang, X. L.; Wang, G.; Wei, F.; Lu, Y. F. Building Robust Architectures of Carbon and Metal Oxide Nanocrystals toward High-Performance Anodes for Lithium-Ion Batteries. *ACS Nano* **2012**, *6*, 9911–9919.
- (41) Liu, H.; Strohbridge, F. C.; Borkiewicz, O. J.; Wiaderek, K. M.; Chapman, K. W.; Chupas, P. J.; Grey, C. P. Capturing Metastable Structures during High-Rate Cycling of  $\text{LiFePO}_4$  Nanoparticle Electrodes. *Science* **2014**, *344* (6191), 125817.
- (42) Zhang, X.; van Hulzen, M.; Singh, D. P.; Brownrigg, A.; Wright, J. P.; van Dijk, N. H.; Wagemaker, M. Rate-Induced Solubility and Suppression of the First-Order Phase Transition in Olivine  $\text{LiFePO}_4$ . *Nano Lett.* **2014**, *14*, 2279–2285.
- (43) Niu, J.; Kushima, A.; Qian, X.; Qi, L.; Xiang, K.; Chiang, Y. M.; Li, J. In Situ Observation of Random Solid Solution Zone in  $\text{LiFePO}_4$  Electrode. *Nano Lett.* **2014**, *14*, 4005–4010.
- (44) Sun, H.; Xin, G.; Hu, T.; Yu, M.; Shao, D.; Sun, X.; Lian, J. High-Rate Lithiation-Induced Reactivation of Mesoporous Hollow Spheres for Long-Lived Lithium-Ion Batteries. *Nat. Commun.* **2014**, *5*, 4526.